



## OPEN ACCESS

## EDITED BY

Kevin Koch,  
Medical College of Wisconsin, United States

## REVIEWED BY

Jacopo Falco,  
IRCCS Carlo Besta Neurological Institute  
Foundation, Italy  
Matteo Figini,  
University College London, United Kingdom

## \*CORRESPONDENCE

Hongbin Zheng  
✉ zhb13383728539@163.com  
Jingliang Cheng  
✉ fccchengjl@zzu.edu.cn  
Guohua Zhao  
✉ ghzhao@ha.edu.cn

<sup>†</sup>These authors share first authorship

RECEIVED 23 February 2025

ACCEPTED 08 July 2025

PUBLISHED 23 July 2025

## CITATION

Zhao S, Ma X, Li L, Gao E, Zhao K, Wang M,  
Yang G, Zheng H, Cheng J and Zhao G (2025)  
Histogram analysis based on DTI and NODDI  
for differentiating atypical high-grade glioma  
from primary central nervous system  
lymphoma.  
*Front. Neurol.* 16:1577811.  
doi: 10.3389/fneur.2025.1577811

## COPYRIGHT

© 2025 Zhao, Ma, Li, Gao, Zhao, Wang, Yang,  
Zheng, Cheng and Zhao. This is an  
open-access article distributed under the  
terms of the [Creative Commons Attribution  
License \(CC BY\)](https://creativecommons.org/licenses/by/4.0/). The use, distribution or  
reproduction in other forums is permitted,  
provided the original author(s) and the  
copyright owner(s) are credited and that the  
original publication in this journal is cited, in  
accordance with accepted academic  
practice. No use, distribution or reproduction  
is permitted which does not comply with  
these terms.

# Histogram analysis based on DTI and NODDI for differentiating atypical high-grade glioma from primary central nervous system lymphoma

Shanshan Zhao<sup>1,2†</sup>, Xiaoyue Ma<sup>1,2†</sup>, Linlin Li<sup>3</sup>, Eryuan Gao<sup>1,2</sup>,  
Kai Zhao<sup>1,2</sup>, Mengzhu Wang<sup>4</sup>, Guang Yang<sup>5</sup>, Hongbin Zheng<sup>6\*</sup>,  
Jingliang Cheng<sup>1,2\*</sup> and Guohua Zhao<sup>1,2\*</sup>

<sup>1</sup>Department of Magnetic Resonance Imaging, The First Affiliated Hospital of Zhengzhou University, Zhengzhou, China, <sup>2</sup>Tianjian Laboratory of Advanced Biomedical Sciences, Zhengzhou, China, <sup>3</sup>Dengfeng Hospital of Traditional Chinese Medicine, Dengfeng, China, <sup>4</sup>MR Research Collaboration, Siemens Healthineers Ltd., Beijing, China, <sup>5</sup>Shanghai Key Laboratory of Magnetic Resonance, East China Normal University, Shanghai, China, <sup>6</sup>The Affiliated Hospital of Youjiang Medical University for Nationalities, Baise, China

**Background and purpose:** Distinguishing between high-grade glioma (HGG) and primary central nervous system lymphoma (PCNSL) is of paramount clinical importance, as these entities necessitate substantially different therapeutic approaches. The differential diagnosis becomes particularly challenging when HGG presents without characteristic magnetic resonance imaging (MRI) features, making it difficult to differentiate from PCNSL. The diffusion tensor imaging (DTI) and neurite orientation dispersion and density imaging (NODDI) offer quantitative assessments of water molecule diffusion within tissues, thereby providing potential means to characterize microstructural differences between HGG and PCNSL. This study aims to evaluate the diagnostic efficacy of histogram analysis based on DTI and NODDI parameters in differentiating atypical HGG from PCNSL.

**Materials and methods:** We retrospectively reviewed patients who underwent multi-*b*-value diffusion-weighted imaging (DWI) at our institution. The multi-*b*-value DWI was performed using a single-shot echo-planar imaging (EPI) sequence with six *b*-values (0, 500, 1,000, 1,500, 2,000, and 2,500 s/mm<sup>2</sup>) distributed across 30 directions. The DTI and NODDI model were employed to derive the parametric maps of apparent diffusion coefficient (ADC), fractional anisotropy (FA), intracellular volume fraction (ICVF), isotropic volume fraction (ISOVF), and orientation dispersion index (ODI). Two regions of interest (ROIs) were manually delineated within the enhancing tumor area and the peritumoral edema. Histogram features were extracted from these ROIs. Comparisons between HGG and PCNSL were performed. Receiver operating characteristic (ROC) curves were drawn, and the area under the curve (AUC), sensitivity, specificity, and accuracy were calculated. *p* < 0.05 was considered statistically significant.

**Results:** A total of 55 patients (30 with atypical HGG and 25 with PCNSL), were included in this study. Several histogram features of parameters could be used to classify the HGG and PCNSL (*p* < 0.05). The 75th percentile of the orientation dispersion index (ODI<sub>75th</sub>) within the enhancing tumor region demonstrated the highest diagnostic performance (AUC = 0.985). At an optimal threshold of 0.604, ODI<sub>75th</sub> yielded a sensitivity of 96%, a specificity of 93.33%, and an accuracy of 94.55% for distinguishing HGG from PCNSL.

**Conclusion:** DTI-and NODDI-based histogram analysis demonstrates the potential to differentiate between atypical HGG and PCNSL.  $ODI_{75th}$  within the enhancing tumor region showed the most favorable diagnostic performance.

#### KEYWORDS

magnetic resonance imaging, neurite orientation dispersion and density imaging, histogram analysis, high-grade glioma, primary central nervous system lymphoma

## 1 Introduction

Glioma and primary central nervous system lymphoma (PCNSL) are two common malignant primary brain tumors (1). Precise diagnosis is of great significance as the therapeutic strategies differ. PCNSLs are not recommended for surgery but rather receive chemotherapy, with or without irradiation, after biopsy. Meanwhile, HGGs necessitate surgical resection followed by concurrent chemoradiation (2–4). Magnetic resonance imaging (MRI) acts as the standard approach for brain tumor diagnosis. Most primary central nervous system lymphomas (PCNSLs) typically appear as homogeneously hyperintense lesions on T2-weighted images and rarely exhibit central necrosis. In contrast, high-grade gliomas (HGGs) are often associated with imaging features such as central necrosis, hemorrhage, or ring-like enhancement, which generally facilitate their diagnosis (5). However, it has been reported that approximately 22.2% of HGGs do not show obvious intra-tumoral necrosis (6), and about 4.4% of PCNSLs may present with ring enhancement, potentially complicating differential diagnosis in atypical cases (7). Distinguishing HGG from PCNSL can be challenging when conventional MRI features are atypical. To address this challenge, researchers are actively exploring advanced imaging analysis techniques (8) and functional MRI (9). Diffusion MRI can provide information on the tissue microenvironment and help in diagnosis. The single-exponential model diffusion-weighted imaging (DWI), diffusion tensor imaging (DTI), and diffusion kurtosis imaging (DKI) have been utilized to differentiate HGG from PCNSL (4, 10–12). Advanced diffusion models have shown promising clinical applications. Recently, the neurite orientation dispersion and density imaging (NODDI) model (13) has garnered attention among radiologists (14). NODDI has been applied in glioma grading (15), genotyping (16), and differential diagnosis (17–19). In this research, we investigate the application of DTI-and NODDI-based histogram analysis for differentiating atypical HGG from PCNSL.

## 2 Materials and methods

This retrospective study was approved by the Scientific Research and Clinical Trial Ethics Committee of the First Affiliated Hospital of Zhengzhou University, and informed consent was waived due to the purely retrospective analysis (Approval Number: 2019-KY-231).

### 2.1 Study participants

A total of 210 patients were included in this study between September 2018 and October 2022, who underwent MRI including routine sequences and multi-*b*-value diffusion-weighted imaging (DWI), and were pathologically diagnosed with either grade 3–4

glioma (20) or PCNSL according to the 2021 World Health Organization (WHO) classification of central nervous system tumors at our hospital. A total of 155 patients were excluded for: (1) anti-tumor treatment or biopsy prior to MRI scanning ( $n = 3$ ); (2) surgery or biopsy not performed within 2 weeks of the MRI examination ( $n = 6$ ); (3) images reviewed by two radiologists (SZ with 9 years of experience and XM with 11 years of experience) with severe motion or susceptibility artifacts ( $n = 2$ ); (4) lesions with more than 13% necrosis in the enhancing tumor (11) ( $n = 144$ ). Finally, 30 patients with atypical HGG and 25 with PCNSL were recruited.

### 2.2 MRI protocol

All patients were scanned using a 3.0 T MRI scanner (MAGNETOM Prisma; Siemens Healthineers, Erlangen, Germany) with a 64-channel head and neck integrated coil. The imaging sequences included: (1) axial T2 dark-fluid: TR/TE, 8,000/81 ms; FOV,  $220 \times 220 \text{ mm}^2$ ; acquisition matrix,  $314 \times 314$ ; slice thickness, 5.0 mm; (2) axial multi-*b*-value DWI: single-shot echo-planar imaging (EPI) sequence, with five non-zero *b*-values (500, 1,000, 1,500, 2,000, and 2,500  $\text{s/mm}^2$ ) distributed across 30 directions, and one zero *b*-value ( $b = 0 \text{ s/mm}^2$ ); TR/TE, 2,500/71 ms; FOV,  $220 \times 220 \text{ mm}^2$ ; acquisition matrix,  $100 \times 100$ ; slice thickness, 2.2 mm; and 3. 3D contrast-enhanced T1 magnetization-prepared rapid gradient echo (CE-T1 MPRAGE): TR/TE, 2300/2.32 ms; FOV,  $240 \times 240 \text{ mm}^2$ ; acquisition matrix,  $266 \times 266$ ; slice thickness, 0.9 mm. The acquisition time for the multi-*b*-value DWI sequence was 6 min and 34 s. The T1 MPRAGE sequence was performed following the administration of 0.2 mol/kg body weight of gadopentetate dimeglumine (Magnevist, Bayer Schering Pharma AG, Berlin, Germany). All sequences covered the entire brain.

### 2.3 Image processing and analysis

Diffusion Kit Eddy tool<sup>1</sup> (21) was used to perform eddy current and motion correction for the multi-*b*-value DWI images. NeuDilab, a software based on DIPY<sup>2</sup> (22), was used for post-processing for the multi-*b*-value DWI images. The apparent diffusion coefficient (ADC), fractional anisotropy (FA), intracellular volume fraction (ICVF), isotropic volume fraction (ISOVF), and orientation dispersion index (ODI) were calculated. CE-T1 MPRAGE images and all parametric maps were registered to the axial T2 dark-fluid images. Two regions of interest (ROIs) were manually delineated with reference to the

<sup>1</sup> <https://diffusionkit.readthedocs.io>

<sup>2</sup> <http://nipy.org/>

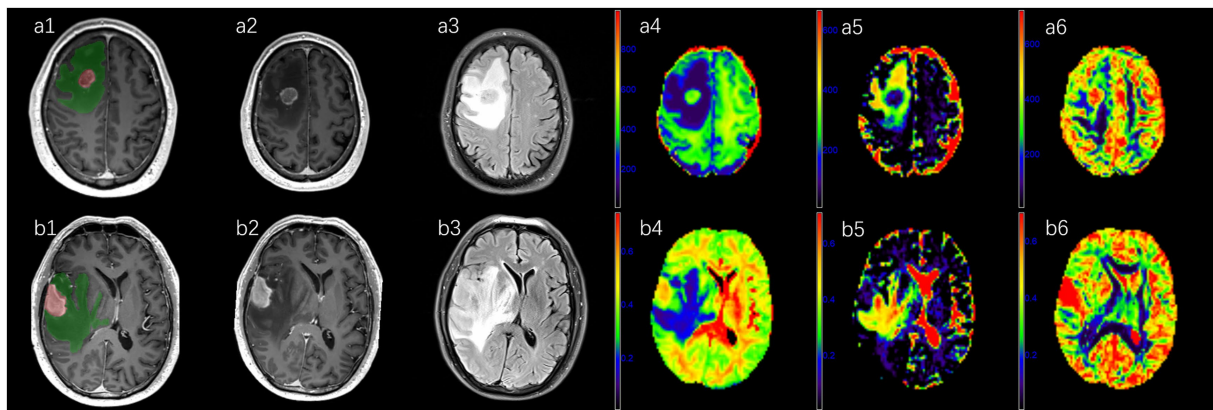


FIGURE 1

A 62-year-old male diagnosed with atypical high-grade glioma in the right frontal lobe (a1–a6) and a 59-year-old male diagnosed with primary central nervous system lymphoma in the right temporal lobe (b1–b6). CE-T1-MPRAGE (a2,b2) and T2-tirm-dark-fluid (a3,b3) images depict peritumoral edema in green and the enhancing area in red (a1,b1). Parametric maps of NODDI (a4–a6,b4–b6) include intracellular volume fraction (a4,b4), isotropic volume fraction (a5,b5) and orientation dispersion index (a6,b6).

CE-T1 MPRAGE and T2 dark-fluid images by two radiologists (SZ with 9 years of experience and XM with 11 years of experience), who were blinded to the pathological results. The enhancing tumor area (ROI 1) was outlined on the registered CE-T1 MPRAGE images across all slices (Figure 1), excluding cystic, necrotic, and hemorrhagic regions. Peritumoral edema (ROI 2) was defined as the area surrounding the enhancing tumor margin with high signal intensity on all slices of the T2 dark-fluid images (Figure 1). Registration and delineation were performed using ITK-SNAP software (version 3.8.0, <http://www.itksnap.org>) (23). The two ROIs and all parametric maps were imported into MATLAB (version. R2017b; MathWorks, Natick, MA, United States) to compute histogram features of parameters in each ROI, including minimum (min), mean, maximum (max), 10th percentile (10th), 25th percentile (25th), median, 75th percentile (75th), 90th percentile (90th), variance, skewness, and kurtosis.

## 2.4 Statistical analyses

Statistical analyses were conducted using SPSS software (version 21.0; SPSS Inc., Chicago, IL, United States). The normality of all histogram parameters was assessed using the Shapiro–Wilk test, and the homogeneity of variance was evaluated using Levene’s test. Data conforming to a normal distribution were presented as mean  $\pm$  standard deviation, while non-normally distributed data were expressed as median (25th, 75th). Comparative analysis between the atypical HGG and PCNSL groups was performed using an independent *t*-test for normally distributed data with uniform variance, while the Mann–Whitney *U* test was used for the remaining datasets. Statistical significance was set at  $p < 0.05$ . Benjamini–Hochberg correction was applied to adjust the *p*-values of diffusion parameters for multiple comparisons. Receiver operating characteristic (ROC) analyses were conducted to evaluate the diagnostic efficiency of parameters showing significant differences. Areas under the curve (AUCs) were measured, and the corresponding sensitivity, specificity, and accuracy were calculated by selecting the cut-off value with the maximum Youden index.

## 3 Results

### 3.1 Patient demographics

Among the 55 patients, 30 were diagnosed with atypical HGG (18 males, 12 females; age range, 20–73 years; mean age,  $51 \pm 12$  years), and 25 patients had PCNSL (14 males, 11 females; age range, 33–72 years; mean age,  $59 \pm 9$  years). All cases were classified according to the 2021 WHO criteria. In the atypical HGG group, 26 patients were diagnosed with glioblastoma, IDH-wildtype (WHO grade 4), 2 with astrocytoma, IDH-mutant (WHO grade 3), and 2 with oligodendroglioma, IDH-mutant and 1p/19q-codeleted (WHO grade 3). All patients in the PCNSL group were diagnosed with large B-cell lymphoma.

### 3.2 Histogram parameter values in the enhancing area

The histogram parameter (ADC, FA, ICVF, ISOVF, and ODI) in the enhancing area are shown in Table 1 and Figure 2. In the enhancing area,  $ADC_{\text{variance}}$ ,  $FA_{\text{kurtosis}}$ ,  $FA_{\text{skewness}}$ ,  $ICVF_{\text{mean}}$ ,  $ICVF_{\text{max}}$ ,  $ICVF_{10\text{th}}$ ,  $ICVF_{25\text{th}}$ ,  $ICVF_{\text{median}}$ ,  $ICVF_{75\text{th}}$ ,  $ICVF_{90\text{th}}$ ,  $ICVF_{\text{variance}}$ ,  $ISOVF_{\text{mean}}$ ,  $ISOVF_{\text{max}}$ ,  $ISOVF_{10\text{th}}$ ,  $ISOVF_{25\text{th}}$ ,  $ISOVF_{\text{median}}$ ,  $ISOVF_{75\text{th}}$ ,  $ISOVF_{90\text{th}}$ ,  $ODI_{\text{mean}}$ ,  $ODI_{\text{max}}$ ,  $ODI_{10\text{th}}$ ,  $ODI_{25\text{th}}$ ,  $ODI_{\text{median}}$ ,  $ODI_{75\text{th}}$ ,  $ODI_{90\text{th}}$  and  $ODI_{\text{variance}}$  were significantly lower for atypical HGG than for PCNSL, whereas  $ADC_{10\text{th}}$ ,  $ADC_{25\text{th}}$ ,  $ADC_{\text{median}}$ ,  $ADC_{\text{minimum}}$ ,  $ADC_{\text{mean}}$ ,  $FA_{10\text{th}}$ ,  $FA_{25\text{th}}$ ,  $FA_{\text{median}}$ ,  $FA_{75\text{th}}$ ,  $FA_{90\text{th}}$ ,  $FA_{\text{minimum}}$ ,  $FA_{\text{mean}}$ ,  $ICVF_{\text{skewness}}$  and  $ODI_{\text{skewness}}$  were significantly higher for atypical HGG than for PCNSL ( $p < 0.05$ ). The  $ISOVF_{\text{min}}$  values of atypical HGG and PCNSL were both  $< 0.001$ ; therefore, no comparison was made.

### 3.3 Histogram parameter values in peritumoral edema

Table 2 and Figure 3 illustrate the histogram parameter values (ADC, FA, ICVF, ISOVF, and ODI) for peritumoral edema. In this

TABLE 1 Histogram parameter values in the enhancing area.

Parameter	HGG	PCNSL	<i>t/U</i> value	Adjusted <i>p</i>
ADC <sub>10th</sub>	0.872 ± 0.162	0.712 ± 0.149	3.765 <sup>a</sup>	<0.001***
ADC <sub>25th</sub>	0.946 ± 0.187	0.789 ± 0.138	3.501 <sup>a</sup>	0.002**
ADC <sub>median</sub>	1.046 ± 0.218	0.905 ± 0.148	2.737 <sup>a</sup>	0.013*
ADC <sub>minimum</sub>	0.721 (0.62, 0.823)	0.557 (0.437, 0.646)	604.5 <sup>c</sup>	<0.001***
ADC <sub>mean</sub>	1.073 ± 0.216	0.958 ± 0.146	2.348 <sup>b</sup>	0.031*
ADC <sub>variance</sub>	0.029 (0.02, 0.054)	0.049 (0.032, 0.068)	220 <sup>c</sup>	0.013*
FA <sub>10th</sub>	0.103 (0.076, 0.164)	0.046 (0.036, 0.058)	688 <sup>c</sup>	<0.001***
FA <sub>25th</sub>	0.139 (0.098, 0.205)	0.059 (0.046, 0.084)	689 <sup>c</sup>	<0.001***
FA <sub>median</sub>	0.194 ± 0.075	0.095 ± 0.034	6.488 <sup>b</sup>	<0.001***
FA <sub>75th</sub>	0.245 ± 0.092	0.15 ± 0.051	4.834 <sup>b</sup>	<0.001***
FA <sub>90th</sub>	0.292 ± 0.107	0.227 ± 0.082	2.487 <sup>a</sup>	0.023*
FA <sub>minimum</sub>	0.051 (0.029, 0.077)	0.016 (0.011, 0.022)	675 <sup>c</sup>	<0.001***
FA <sub>mean</sub>	0.202 ± 0.076	0.12 ± 0.039	5.114 <sup>b</sup>	<0.001***
FA <sub>skewness</sub>	0.55 (0.121, 0.863)	1.656 (1.404, 2.036)	74 <sup>c</sup>	<0.001***
FA <sub>kurtosis</sub>	2.92 (2.532, 3.997)	5.523 (4.148, 7.874)	111 <sup>c</sup>	<0.001***
ICVF <sub>10th</sub>	0.235 ± 0.088	0.304 ± 0.084	−2.944 <sup>a</sup>	0.008**
ICVF <sub>25th</sub>	0.272 ± 0.097	0.393 ± 0.093	−4.729 <sup>a</sup>	<0.001***
ICVF <sub>median</sub>	0.33 ± 0.105	0.487 ± 0.117	−5.232 <sup>a</sup>	<0.001***
ICVF <sub>75th</sub>	0.358 (0.316, 0.437)	0.581 (0.467, 0.617)	108 <sup>c</sup>	<0.001***
ICVF <sub>90th</sub>	0.437 ± 0.121	0.622 ± 0.144	−5.162 <sup>a</sup>	<0.001***
ICVF <sub>mean</sub>	0.334 ± 0.099	0.474 ± 0.102	−5.149 <sup>a</sup>	<0.001***
ICVF <sub>max</sub>	0.596 (0.463, 0.852)	0.93 (0.677, 0.986)	192 <sup>c</sup>	0.003**
ICVF <sub>variance</sub>	0.006 (0.002, 0.013)	0.013 (0.008, 0.02)	191 <sup>c</sup>	0.003**
ICVF <sub>skewness</sub>	0.484 (−0.065, 0.93)	−0.094 (−0.457, 0.213)	562 <sup>c</sup>	0.003**
ISOVF <sub>10th</sub>	0.002 (0.001, 0.008)	0.017 (0.01, 0.038)	151 <sup>c</sup>	<0.001***
ISOVF <sub>25th</sub>	0.011 (0.006, 0.044)	0.051 (0.041, 0.088)	163 <sup>c</sup>	<0.001***
ISOVF <sub>median</sub>	0.047 (0.026, 0.104)	0.106 (0.086, 0.166)	190 <sup>c</sup>	0.003**
ISOVF <sub>75th</sub>	0.135 (0.072, 0.207)	0.187 (0.153, 0.262)	217 <sup>c</sup>	0.011*
ISOVF <sub>90th</sub>	0.259 (0.116, 0.315)	0.308 (0.243, 0.447)	232 <sup>c</sup>	0.022*
ISOVF <sub>mean</sub>	0.1 (0.049, 0.148)	0.14 (0.112, 0.21)	213 <sup>c</sup>	0.009**
ISOVF <sub>max</sub>	0.536 ± 0.232	0.726 ± 0.187	−3.3 <sup>a</sup>	0.003**
ODI <sub>10th</sub>	0.236 ± 0.079	0.334 ± 0.107	−3.902 <sup>a</sup>	<0.001***
ODI <sub>25th</sub>	0.297 ± 0.073	0.476 ± 0.126	−6.261 <sup>b</sup>	<0.001***
ODI <sub>median</sub>	0.372 ± 0.081	0.646 ± 0.118	−9.824 <sup>b</sup>	<0.001***
ODI <sub>75th</sub>	0.458 ± 0.092	0.768 ± 0.095	−12.221 <sup>a</sup>	<0.001***
ODI <sub>90th</sub>	0.534 (0.445, 0.637)	0.859 (0.774, 0.882)	13 <sup>c</sup>	<0.001***
ODI <sub>mean</sub>	0.382 ± 0.075	0.611 ± 0.098	−9.815 <sup>a</sup>	<0.001***
ODI <sub>max</sub>	0.725 (0.658, 0.818)	0.933 (0.919, 0.946)	25 <sup>c</sup>	<0.001***
ODI <sub>variance</sub>	0.013 (0.008, 0.019)	0.035 (0.027, 0.044)	49 <sup>c</sup>	<0.001***
ODI <sub>skewness</sub>	0.356 ± 0.417	−0.592 ± 0.439	8.188 <sup>a</sup>	<0.001***

<sup>a</sup>Data followed a normal distribution with homogeneity of variance; independent *t*-test was used.

<sup>b</sup>Data followed a normal distribution without homogeneity of variance; Welch's *t*-test was used.

<sup>c</sup>Data did not follow a normal distribution; Mann–Whitney *U* test was used. \*0.01 < *p* ≤ 0.05; \*\*0.001 < *p* ≤ 0.01; \*\*\**p* ≤ 0.001.



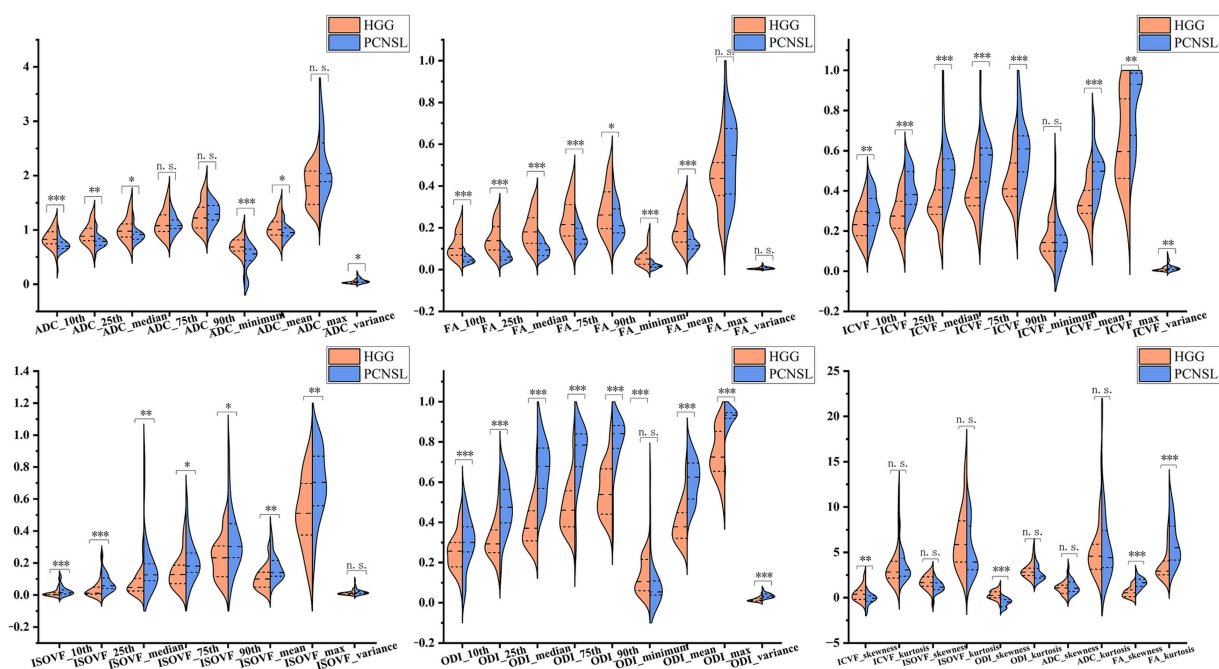


FIGURE 2

Violin graphs of histogram parameter values in the enhancing area. HGG, high-grade glioma; ADC, apparent diffusion coefficient; FA, fractional anisotropy; ICVF, intracellular volume fraction; ISOVF, isotropic volume fraction; ODI, orientation dispersion index; PCNSL, primary central nervous system lymphoma. \* $0.01 < p \leq 0.05$ ; \*\* $0.001 < p \leq 0.01$ ; \*\*\* $p \leq 0.001$ . n.s., no significance.

area, the values of  $ADC_{10th}$ ,  $ADC_{25th}$ ,  $ADC_{median}$ ,  $ADC_{75th}$ ,  $ADC_{90th}$ ,  $ADC_{mean}$ ,  $ISOVF_{mean}$ ,  $ISOVF_{10th}$ ,  $ISOVF_{25th}$ ,  $ISOVF_{median}$ ,  $ISOVF_{75th}$ ,  $ISOVF_{90th}$ ,  $ISOVF_{variance}$ ,  $ODI_{max}$ ,  $ODI_{variance}$  and  $ODI_{skewness}$  were significantly lower for atypical HGG compared to PCNSL. Conversely,  $ADC_{skewness}$ ,  $ADC_{kurtosis}$ ,  $ISOVF_{skewness}$ ,  $ISOVF_{kurtosis}$ ,  $ODI_{mean}$ ,  $ODI_{10th}$ ,  $ODI_{25th}$  and  $ODI_{median}$ ,  $ODI_{75th}$  were significantly higher for atypical HGG compared to PCNSL ( $p < 0.05$ ). As both the  $ISOVF_{min}$  of atypical HGG and PCNSL were  $< 0.001$ , a comparison was not conducted.

### 3.4 Performance of histogram parameters from both ROIs in differentiating atypical HGG from PCNSL

Table 3 presents the ROC analyses of all significant histogram parameter values in the enhancing areas. Figures 4A,B present the ROC curves of the histogram parameters with the highest AUC from each model in the enhancing and peritumoral edema regions, respectively. Notably, the  $ODI_{75th}$  displayed the highest AUC of 0.985 [95% confidence interval (CI): 0.957–1.000] with an accuracy of 0.945 (52/55) at the optimal threshold of 0.604. Its corresponding sensitivity and specificity were 0.96 and 0.933, respectively. The AUC of the other parameters ranged from 0.655–0.983.

Table 4 display the ROC analyses of all significant histogram parameter values for peritumoral edema. In this context, the  $ISOVF_{10th}$  exhibited the highest AUC of 0.921 (95% CI: 0.839–0.98) with an accuracy of 0.891 (49/55) at an optimal threshold of 0.009. The corresponding sensitivity and specificity were 0.96 and 0.833, respectively. The AUCs for the remaining parameters ranged from 0.681–0.900.

## 4 Discussion

In this study, we evaluated the diagnostic value of DTI- and NODDI-based histogram analysis in distinguishing between atypical HGG and PCNSL. Multiple histogram parameters in the enhancing area or peritumoral edema were shown to be effective in this discrimination, and the  $ODI_{75th}$  from the enhancing area presented the strongest diagnostic capability.

Histogram-based features have demonstrated high applicability in characterizing highly heterogeneous tumor tissues (24). Compared to conventional summary metrics such as the mean or median,  $ODI_{75th}$  and  $ODI_{90th}$  provide more targeted information about regions where white matter fiber tracts are substantially disrupted by tumor infiltration. Unlike extreme values (e.g., maximum or minimum), close to percentiles are less susceptible to noise and contamination caused by errors in VOI delineation or image registration (15, 25), notably, among the histogram-derived parameters of FA,  $FA_{25th}$  and  $FA_{90th}$  exhibited the highest AUC values. Given the mathematically inverse relationship between FA and ODI (13), parameters such as  $FA_{25th/10th}$  and  $ODI_{75th/90th}$  may reflect similar tumor subregions—specifically, regions within the tumor parenchyma where axonal fibers demonstrate pronounced alterations, including crossing, curving, or disorganization. Alterations in intra-tumoral neural fiber tracts are difficult to observe with conventional MRI but can be detected using advanced diffusion magnetic resonance techniques, which can subsequently be employed to characterize the tumor's growth behavior. ODI reflects the spread of neurite orientation. It can portray the microstructural complexity, particularly the bending of white matter axons and the pattern of gray matter dendrite expansion (13, 26, 27). We found ODI values are lower and FA values are higher in

TABLE 2 Histogram parameter values in the peritumoral edema.

Parameter	HGG	PCNSL	<i>t/U</i> value	Adjusted <i>p</i>
ADC <sub>10th</sub>	0.808 ± 0.078	0.889 ± 0.096	−3.45 <sup>a</sup>	0.003**
ADC <sub>25th</sub>	0.912 ± 0.122	1.056 ± 0.146	−3.996 <sup>a</sup>	<0.001***
ADC <sub>median</sub>	1.027 (0.898, 1.238)	1.302 (1.139, 1.409)	170 <sup>c</sup>	0.002**
ADC <sub>75th</sub>	1.183 (1.014, 1.462)	1.522 (1.361, 1.667)	181 <sup>c</sup>	0.003**
ADC <sub>90th</sub>	1.353 (1.193, 1.631)	1.677 (1.615, 1.87)	182.5 <sup>c</sup>	0.003**
ADC <sub>mean</sub>	1.096 ± 0.187	1.284 ± 0.175	−3.824 <sup>a</sup>	0.002**
ADC <sub>skewness</sub>	0.968 (0.217, 1.645)	0.035 (−0.211, 0.382)	592 <sup>c</sup>	<0.001***
ADC <sub>kurtosis</sub>	5.054 (2.563, 9.985)	2.405 (2.22, 2.884)	575 <sup>c</sup>	0.002**
ISOVF <sub>10th</sub>	0.003 (0.001, 0.007)	0.025 (0.016, 0.049)	59 <sup>c</sup>	<0.001***
ISOVF <sub>25th</sub>	0.016 (0.007, 0.042)	0.083 (0.064, 0.13)	75 <sup>c</sup>	<0.001***
ISOVF <sub>median</sub>	0.059 (0.032, 0.136)	0.175 (0.15, 0.233)	116 <sup>c</sup>	<0.001***
ISOVF <sub>75th</sub>	0.124 (0.088, 0.277)	0.291 (0.258, 0.389)	151 <sup>c</sup>	<0.001***
ISOVF <sub>90th</sub>	0.29 ± 0.162	0.427 ± 0.108	−3.737 <sup>b</sup>	0.002**
ISOVF <sub>mean</sub>	0.102 (0.07, 0.177)	0.203 (0.181, 0.264)	130 <sup>c</sup>	<0.001***
ISOVF <sub>variance</sub>	0.016 (0.007, 0.025)	0.021 (0.018, 0.031)	239 <sup>c</sup>	0.047*
ISOVF <sub>skewness</sub>	1.891 ± 1.137	0.753 ± 0.687	4.575 <sup>b</sup>	<0.001***
ISOVF <sub>kurtosis</sub>	7.089 (3.258, 13.015)	3.105 (2.215, 4.453)	567 <sup>c</sup>	0.003**
ODI <sub>10th</sub>	0.154 ± 0.062	0.097 ± 0.03	4.439 <sup>b</sup>	<0.001***
ODI <sub>25th</sub>	0.223 ± 0.066	0.157 ± 0.044	4.436 <sup>b</sup>	<0.001***
ODI <sub>median</sub>	0.308 ± 0.064	0.251 ± 0.045	3.748 <sup>a</sup>	0.002**
ODI <sub>75th</sub>	0.39 (0.355, 0.439)	0.344 (0.332, 0.393)	535 <sup>c</sup>	0.016*
ODI <sub>mean</sub>	0.314 ± 0.058	0.27 ± 0.038	3.247 <sup>a</sup>	0.005**
ODI <sub>max</sub>	0.781 ± 0.094	0.86 ± 0.077	−3.397 <sup>a</sup>	0.003**
ODI <sub>variance</sub>	0.017 (0.013, 0.019)	0.019 (0.018, 0.023)	182 <sup>c</sup>	0.003**
ODI <sub>skewness</sub>	0.257 ± 0.336	0.656 ± 0.245	−4.934 <sup>a</sup>	<0.001***

<sup>a</sup>Data followed a normal distribution with homogeneity of variance; independent *t*-test was used.  
<sup>b</sup>Data followed a normal distribution without homogeneity of variance; Welch's *t*-test was used.  
<sup>c</sup>Data did not follow a normal distribution; Mann–Whitney *U* test was used. \*0.01 < *p* ≤ 0.05; \*\*0.001 < *p* ≤ 0.01; \*\*\**p* ≤ 0.001.

atypical HGG than in PCNSL. Previous study also indicated significantly higher FA in HGG compared to PCNSL (28), which is attributed to the disparity in the quantity of nerve fibers between the two tumors. However, explaining the parameter variations solely by the difference in neurite density might lead to a conflict between the two parameters, ODI and ICVF. In our study, atypical HGG displayed conspicuously lower ICVF values in contrast to PCNSL. Higher ICVF skewness in atypical HGG complementarily indicates the trend of lower ICVF values distribution in HGG. As per the definition of the NODDI model, water diffusion within voxels is partitioned into separate contributions from three compartments, with ICVF being the fraction of intracellular volume within voxels, representing neurite density (27). This variance might be ascribed to the presence of microcysts in HGG (30) and the relatively high neurite density in PCNSL (31). Würtemberger et al. (14) confirmed the higher axonal density in PCNSL with histological evidence. Considering our results and evidence presented in these studies, we propose that while more axonal structures are preserved within PCNSL, the tumor's expansive growth displaces, compresses, and intersects with fibrous structures, leading to a decrease in isotropy. In HGG, due to its invasive growth pattern, extensive fiber destruction occurs, leaving the remaining

fibrous structures with greater directionality. Consequently, ODI is lower in HGG. In the study by Würtemberger et al. (14), a similar trend in ODI was observed, but without statistical significance, likely due to the limited sample size. ISOVF represents an isotropic diffusion signal from the cerebrospinal fluid compartment, and deviations in ISOVF values suggest a higher content of free water in PCNSL tissues. However, these findings are inconsistent with those reported by Würtemberger et al. (14). In both our study and theirs, the role of ISOVF in differential diagnosis appears limited, as evidenced by its relatively low AUC value. This suggests that the diagnostic utility of ISOVF remains uncertain and warrants further validation in studies with larger sample sizes. Lower ADC values in PCNSL suggest higher cellularity compared to HGG, which has been histologically confirmed in Haopeng et al. (29) study.

ODI demonstrated superior diagnostic performance compared to FA, largely owing to the NODDI model's ability to more specifically represent white matter fiber architecture (13). FA is influenced by a variety of factors, including fiber orientation coherence and neurite density. In PCNSL, the disruption and displacement of white matter tracts typically result in a reduction of FA, while high neurite density can increase FA. These opposing effects may partially cancel each

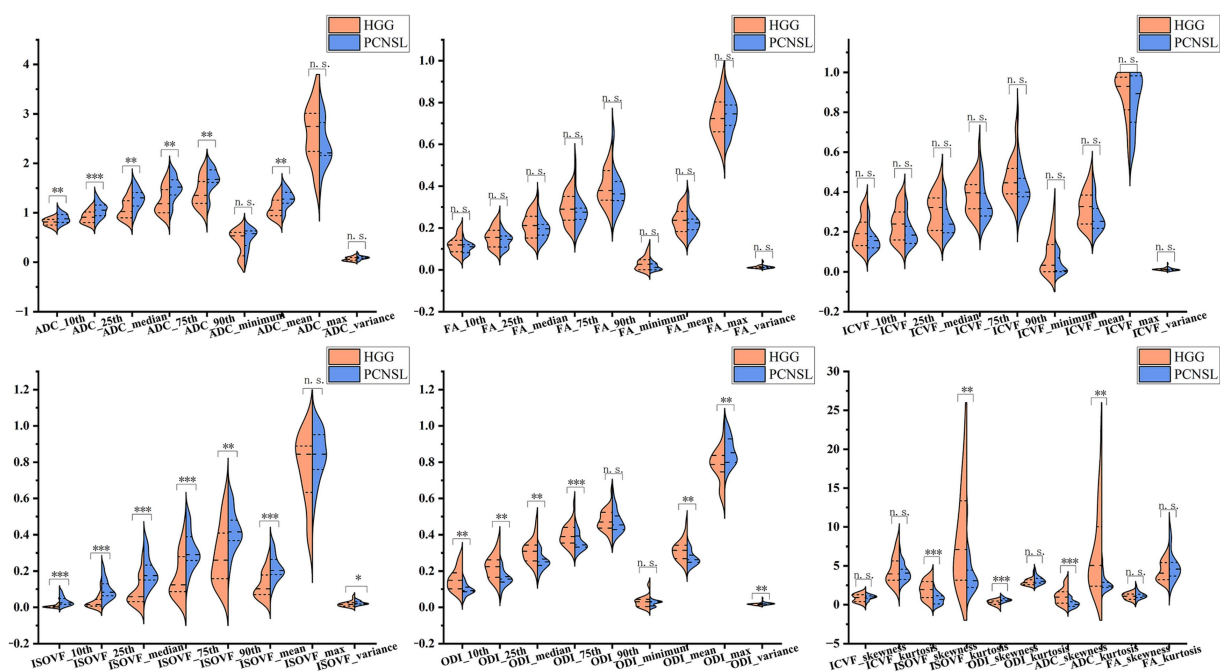


FIGURE 3

Violin graphs of histogram parameter values in the peritumoral edema. HGG, high-grade glioma; ADC, apparent diffusion coefficient; FA, fractional anisotropy; ICVF, intracellular volume fraction; ISOVF, isotropic volume fraction; ODI, orientation dispersion index; PCNSL, primary central nervous system lymphoma. \* $0.01 < p \leq 0.05$ ; \*\* $0.001 < p \leq 0.01$ ; \*\*\* $p \leq 0.001$ . n.s., no significance.

other out, thereby reducing the discriminatory power of FA in differentiating PCNSL from HGG. In contrast, the NODDI model decomposes these microstructural changes into distinct parameters: ICVF reflects neurite density, and ODI quantifies the orientation dispersion of fibers. By isolating orientation dispersion from confounding factors such as cellular density, ODI provides a more robust metric that more accurately reflects the architectural disorganization characteristic of PCNSL, yielding a clearer distinction from HGG.

However, the biological interpretation of NODDI-derived parameters in tumor tissue remains largely empirical and requires further histological validation. This model was originally designed to characterize white matter microstructure in healthy or neurodegenerative brains—such as in neonates or patients with dementia (32)—and lacks explicit modeling for neoplastic components. Neoplastic cells may exhibit restricted diffusion similar to that of neurites, and thus may be erroneously classified into the intracellular compartment, resulting in an artificial elevation of ICVF. This misclassification could misleadingly suggest preserved neuronal integrity in regions actually dominated by tumor cells. Similarly, the disorganized microstructure introduced by malignant proliferation may be interpreted as increased neurite dispersion, contributing to inflated ODI values. Moreover, the NODDI model does not account for perfusion effects, which are commonly observed in highly vascularized tumors. This becomes particularly problematic at lower  $b$ -values: in our protocol, the inclusion of a  $b = 500 \text{ s/mm}^2$  shell may have introduced mild perfusion contamination. Fast diffusion components retained at this  $b$ -value may be misclassified as extracellular space, potentially leading to overestimation of ISOVF and underestimation of ICVF. Also, ODI may become unstable due to

contamination by randomly flowing blood signals. Nevertheless, the clinical potential of the NODDI model in tumor diagnostics has been supported by a growing body of research. Quantitative NODDI parameters have been applied in glioma grading and molecular subtype prediction (33, 34), NODDI-based tractography has proven effective in evaluating corticospinal tract (CST) infiltration and damage caused by HGGs (35). Furthermore, multiparametric NODDI radiomic models have demonstrated good performance in the preoperative differentiation of glioblastoma and brain metastases (36). Compared to NODDI, several other diffusion models may offer better theoretical alignment and practical utility for tumor microstructure characterization with their assumptions that are more appropriate for pathological tissues. The vascular, extracellular, and restricted diffusion for cytometry in tumors (VERDICT) model explicitly incorporates perfusion and distinguishes between key microenvironmental components (37), providing estimates for intracellular volume fraction (fIC), vascular volume fraction (fVASC), extracellular-extravascular space (fEES), and cell radius. This enables a more comprehensive representation of tumor cellularity and vascularization. The imaging microstructural parameters using limited spectrally edited diffusion (IMPULSED) model is capable of quantifying cell membrane permeability (38), a parameter increasingly recognized for its value in assessing tumor viability and treatment response. Single-compartment models such as diffusion kurtosis imaging (DKI) and mean apparent propagator MRI (MAP-MRI) yield metrics that reflect tissue heterogeneity, and have shown promise in tumor subtype classification and prediction of molecular phenotypes (34, 39).

NODDI could be more appropriate for characterizing the peritumoral edema region, where the predominant constituents are

TABLE 3 ROC analyses of significant histogram parameters in the enhancing area.

Parameter	AUC (95% CI)	Cut-off value	Sensitivity	Specificity	Accuracy
ADC <sub>10th</sub>	0.773 (0.64, 0.889)	0.8	0.880	0.667	0.764
ADC <sub>25th</sub>	0.755 (0.619, 0.872)	0.868	0.840	0.667	0.745
ADC <sub>median</sub>	0.703 (0.561, 0.836)	0.923	0.680	0.733	0.709
ADC <sub>minimum</sub>	0.806 (0.683, 0.911)	0.607	0.680	0.833	0.764
ADC <sub>mean</sub>	0.655 (0.505, 0.803)	1.072	0.880	0.467	0.655
ADC <sub>variance</sub>	0.707 (0.561, 0.832)	0.03	0.800	0.600	0.691
FA <sub>10th</sub>	0.917 (0.833, 0.979)	0.069	0.920	0.800	0.855
FA <sub>25th</sub>	0.919 (0.84, 0.975)	0.096	0.920	0.767	0.836
FA <sub>median</sub>	0.9 (0.804, 0.964)	0.125	0.840	0.800	0.818
FA <sub>75th</sub>	0.812 (0.691, 0.917)	0.179	0.760	0.767	0.764
FA <sub>90th</sub>	0.684 (0.541, 0.821)	0.214	0.560	0.767	0.673
FA <sub>minimum</sub>	0.9 (0.811, 0.968)	0.025	0.800	0.833	0.818
FA <sub>mean</sub>	0.829 (0.711, 0.925)	0.147	0.800	0.733	0.764
FA <sub>skewness</sub>	0.901 (0.809, 0.971)	1.005	0.920	0.833	0.873
FA <sub>kurtosis</sub>	0.852 (0.736, 0.943)	3.218	1.000	0.667	0.818
ICVF <sub>10th</sub>	0.715 (0.573, 0.845)	0.239	0.800	0.600	0.691
ICVF <sub>25th</sub>	0.815 (0.691, 0.913)	0.296	0.840	0.700	0.764
ICVF <sub>median</sub>	0.855 (0.751, 0.943)	0.337	0.920	0.667	0.782
ICVF <sub>75th</sub>	0.856 (0.748, 0.94)	0.439	0.840	0.767	0.800
ICVF <sub>90th</sub>	0.849 (0.747, 0.94)	0.465	0.920	0.700	0.800
ICVF <sub>mean</sub>	0.847 (0.732, 0.936)	0.356	0.920	0.667	0.782
ICVF <sub>max</sub>	0.744 (0.611, 0.865)	0.493	1.000	0.400	0.673
ICVF <sub>variance</sub>	0.745 (0.609, 0.859)	0.006	0.920	0.533	0.709
ICVF <sub>skewness</sub>	0.749 (0.619, 0.867)	0.428	0.920	0.533	0.709
ISOVF <sub>10th</sub>	0.799 (0.663, 0.913)	0.005	0.880	0.700	0.782
ISOVF <sub>25th</sub>	0.783 (0.653, 0.9)	0.022	0.880	0.700	0.782
ISOVF <sub>median</sub>	0.747 (0.601, 0.871)	0.055	0.960	0.567	0.745
ISOVF <sub>75th</sub>	0.711 (0.567, 0.839)	0.122	0.960	0.500	0.709
ISOVF <sub>90th</sub>	0.691 (0.549, 0.82)	0.165	1.000	0.367	0.655
ISOVF <sub>mean</sub>	0.716 (0.572, 0.841)	0.084	0.960	0.467	0.691
ISOVF <sub>max</sub>	0.733 (0.593, 0.857)	0.601	0.760	0.667	0.709
ODI <sub>10th</sub>	0.783 (0.652, 0.897)	0.3	0.600	0.867	0.745
ODI <sub>25th</sub>	0.897 (0.796, 0.972)	0.333	0.920	0.733	0.818
ODI <sub>median</sub>	0.969 (0.927, 0.996)	0.438	1.000	0.800	0.891
ODI <sub>75th</sub>	0.985 (0.957, 1)	0.604	0.960	0.933	0.945
ODI <sub>90th</sub>	0.983 (0.952, 1)	0.687	0.960	0.933	0.945
ODI <sub>mean</sub>	0.961 (0.908, 0.995)	0.451	0.960	0.833	0.891
ODI <sub>max</sub>	0.967 (0.919, 0.995)	0.86	1.000	0.833	0.909
ODI <sub>variance</sub>	0.935 (0.861, 0.992)	0.024	0.960	0.867	0.909
ODI <sub>skewness</sub>	0.957 (0.899, 0.995)	−0.059	0.880	0.933	0.909

edematous brain parenchyma and infiltrated white matter tracts rather than compact tumor cells. In these regions, the diffusion environment still partially conforms to the assumptions of the NODDI framework ISOVF demonstrated a unique diagnostic value in the peritumoral edema region. Although it did not exhibit the highest diagnostic performance in this study, it holds merit for elucidating the underlying pathophysiological processes and characterizing the microstructural differences in the edema regions of HGG and PCNSL. Its differential diagnostic potential is likely to be further revealed in future large-scale studies that establish



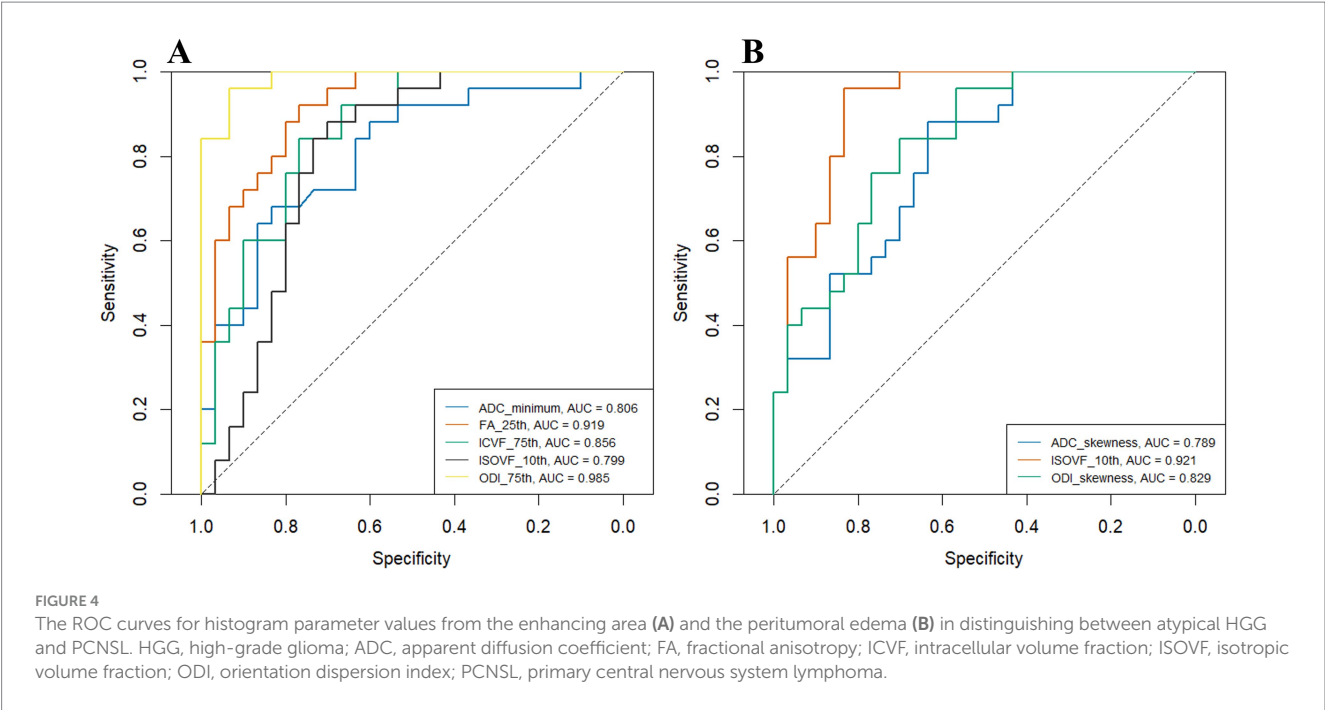


TABLE 4 ROC analyses of significant histogram parameters in the peritumoral edema.

Parameter	AUC (95% CI)	Cut-off value	Sensitivity	Specificity	Accuracy
ADC <sub>10th</sub>	0.734 (0.594, 0.859)	0.867	0.600	0.767	0.691
ADC <sub>25th</sub>	0.778 (0.647, 0.892)	1.04	0.600	0.867	0.745
ADC <sub>median</sub>	0.773 (0.639, 0.885)	1.09	0.880	0.600	0.727
ADC <sub>75th</sub>	0.759 (0.623, 0.884)	1.288	0.880	0.633	0.745
ADC <sub>90th</sub>	0.757 (0.625, 0.884)	1.45	0.880	0.633	0.745
ADC <sub>mean</sub>	0.765 (0.629, 0.883)	1.122	0.880	0.600	0.727
ADC <sub>skewness</sub>	0.789 (0.661, 0.892)	0.851	0.880	0.633	0.745
ADC <sub>kurtosis</sub>	0.767 (0.633, 0.887)	3.478	0.840	0.667	0.745
ISOVF <sub>10th</sub>	0.921 (0.839, 0.98)	0.009	0.960	0.833	0.891
ISOVF <sub>25th</sub>	0.9 (0.809, 0.971)	0.024	1.000	0.700	0.836
ISOVF <sub>median</sub>	0.845 (0.737, 0.939)	0.092	0.960	0.733	0.836
ISOVF <sub>75th</sub>	0.799 (0.672, 0.901)	0.227	0.880	0.700	0.782
ISOVF <sub>90th</sub>	0.764 (0.629, 0.892)	0.328	0.880	0.633	0.745
ISOVF <sub>mean</sub>	0.827 (0.705, 0.925)	0.148	0.880	0.667	0.764
ISOVF <sub>variance</sub>	0.681 (0.535, 0.815)	0.018	0.800	0.567	0.673
ISOVF <sub>skewness</sub>	0.791 (0.66, 0.897)	1.78	0.960	0.567	0.745
ISOVF <sub>kurtosis</sub>	0.756 (0.617, 0.879)	6.065	0.880	0.633	0.745
ODI <sub>10th</sub>	0.796 (0.663, 0.908)	0.127	0.880	0.633	0.745
ODI <sub>25th</sub>	0.799 (0.669, 0.911)	0.199	0.840	0.667	0.745
ODI <sub>median</sub>	0.771 (0.644, 0.887)	0.271	0.800	0.700	0.745
ODI <sub>75th</sub>	0.713 (0.575, 0.847)	0.347	0.640	0.800	0.727
ODI <sub>mean</sub>	0.745 (0.604, 0.868)	0.268	0.640	0.800	0.727
ODI <sub>max</sub>	0.743 (0.605, 0.867)	0.787	0.920	0.533	0.709
ODI <sub>variance</sub>	0.757 (0.62, 0.879)	0.019	0.680	0.733	0.709
ODI <sub>skewness</sub>	0.829 (0.708, 0.921)	0.464	0.840	0.700	0.764

multifactorial models. We noticed significantly lower values of ISOVF, higher ISOVF skewness and ISOVF kurtosis in atypical HGG compared to PCNSL. This disparity might be ascribed to the infiltrative edema characteristic of HGG (40, 41), which comprises infiltrating tumor cells and vasogenic edema. Vasogenic edema mainly results from the tumor's pressure on draining veins, without the presence of tumor cells within the edema (42). In contrast to the 'pure vasogenic edema' (with no infiltrating tumor cells) observed around PCNSL (43), in the peritumoral area of HGG, the infiltrating tumor cells reduce the free water content. ISOVF<sub>10th</sub>, the parameter with the highest diagnostic performance in the edema region (AUC = 0.921), corresponds to areas with relatively low free water content. This effectively reflects the invasive growth behavior of tumor cells in HGG, highlighting its potential as a valuable biomarker for characterizing tumor-related microstructural changes. In the peritumoral edema of atypical HGG, infiltrating tumor cells disrupt nerve fibers, leading to more dispersed water diffusion. This results in higher values for ODI<sub>mean</sub>, ODI<sub>10th</sub>, ODI<sub>25th</sub>, ODI<sub>median</sub>, and ODI<sub>75th</sub> in atypical HGG compared to PCNSL. Interestingly, however, ODI<sub>max</sub> was found to be higher in the edema surrounding PCNSL. This may reflect the characteristics of edematous brain tissue at the tumor-edema interface, where fiber tracts are maximally displaced or intersecting, possibly due to the expansile growth pattern of PCNSL. Such regions may harbor sharply distorted or crossing fibers compressed by the tumor mass rather than infiltrated by tumor cells. Despite this localized increase in ODI<sub>max</sub>, the overall distribution of ODI values is shifted higher in the peritumoral region of HGG, as supported by differences in skewness. These findings underscore the potential of ODI metrics to capture the infiltrative growth behavior of HGG, in contrast to the vasogenic edema in PCNSL, which primarily results from blood-brain barrier disruption with limited tumor infiltration.

This study has several limitations. First, it was conducted at a single center using a single scanner and involved a relatively small sample size. Future studies with larger cohorts, including data from multiple scanners and institutions, are needed to validate these findings. Second, the lack of a validation cohort prevented the development of a multifactorial diagnostic model that integrates parameters from both the edema and enhancement areas. We plan to address this limitation by enrolling more patients in subsequent studies. Third, the interpretation of diffusion parameter changes in this study is empirical and lacks histopathological validation, highlighting the need for future studies incorporating histological correlation.

## 5 Conclusion

DTI-and NODDI-based histogram analysis shows promise in distinguishing between atypical HGG and PCNSL, with the ODI<sub>75th</sub> parameter from the enhancing area demonstrating the best diagnostic performance.

## Data availability statement

The raw data supporting the conclusions of this article will be made available by the authors, without undue reservation.

## Ethics statement

The studies involving humans were approved by the Scientific Research and Clinical Trial Ethics Committee of the First Affiliated Hospital of Zhengzhou University. The studies were conducted in accordance with the local legislation and institutional requirements. The ethics committee/institutional review board waived the requirement of written informed consent for participation from the participants or the participants' legal guardians/next of kin because this study is a purely retrospective analysis.

## Author contributions

SZ: Conceptualization, Writing – original draft. XM: Writing – original draft. LL: Writing – original draft. EG: Writing – original draft. KZ: Writing – original draft. MW: Software, Writing – original draft. GY: Software, Writing – original draft. HZ: Writing – review & editing. JC: Writing – review & editing. GZ: Writing – review & editing.

## Funding

The author(s) declare that financial support was received for the research and/or publication of this article. This study was supported in part by the National Natural Science Foundation of China under Grant 82402395, and in part by the Scientific and Technological Research Project of Henan Province under Grant LHGJ20220403, and in part by the Natural Science Foundation of Henan Province under Grant 232300421298. This study has received funding from the Youth Project of Henan Medical Science and Technology Research Project (Grant No. SBGJ202103078).

## Conflict of interest

Author MW was employed by company Siemens Healthineers Ltd. The remaining authors declare that the research was conducted in the absence of any commercial or financial relationships that could be construed as a potential conflict of interest.

## Generative AI statement

The authors declare that Gen AI was used in the creation of this manuscript. During the preparation of this work, the authors used ChatGPT (OpenAI, Inc.; <https://chatgpt.com/>) to improve the readability and language. After using this tool, the authors reviewed and edited the content as needed and take full responsibility for the content of the publication.

## Publisher's note

All claims expressed in this article are solely those of the authors and do not necessarily represent those of their affiliated organizations, or those of the publisher, the editors and the reviewers. Any product that may be evaluated in this article, or claim that may be made by its manufacturer, is not guaranteed or endorsed by the publisher.

## References

- Lapointe S, Perry A, Butowski NA. Primary brain tumours in adults. *Lancet*. (2018) 392:432–46. doi: 10.1016/S0140-6736(18)30990-5
- Schlegel U. Primary CNS lymphoma. *Ther Adv Neurol Disord*. (2009) 2:93–104. doi: 10.1177/1756285608101222
- Komotar RJ, Otten ML, Moise G, Connolly ES Jr. Radiotherapy plus concomitant and adjuvant temozolomide for glioblastoma—a critical review. *Clin Med Oncol*. (2008) 2:421–2. doi: 10.4137/cmo.s390
- Kickingereder P, Wiestler B, Sahm F, Heiland S, Roethke M, Schlemmer HP, et al. Primary central nervous system lymphoma and atypical glioblastoma: multiparametric differentiation by using diffusion-, perfusion-, and susceptibility-weighted MR imaging. *Radiology*. (2014) 272:843–50. doi: 10.1148/radiol.14132740
- Malikova H, Koubaska E, Weichert J, Klener J, Rulseh A, Liscak R, et al. Can morphological MRI differentiate between primary central nervous system lymphoma and glioblastoma? *Cancer Imaging*. (2016) 16:40. doi: 10.1186/s40644-016-0098-9
- Guo X, Shi Y, Liu D, Li Y, Chen W, Wang Y, et al. Clinical updates on gliomas and implications of the 5th edition of the WHO classification of central nervous system tumors. *Front Oncol*. (2023) 13:1131642. doi: 10.3389/fonc.2023.1131642
- Sutherland T, Yap K, Liew E, Tartaglia C, Pang M, Trost N. Primary central nervous system lymphoma in immunocompetent patients: a retrospective review of MRI features. *J Med Imaging Radiat Oncol*. (2012) 56:295–301. doi: 10.1111/j.1754-9485.2012.02366.x
- Han Y, Wang ZJ, Li WH, Yang Y, Zhang J, Yang XB, et al. Differentiation between primary central nervous system lymphoma and atypical glioblastoma based on MRI morphological feature and signal intensity ratio: a retrospective multicenter study. *Front Oncol*. (2022) 12:811197. doi: 10.3389/fonc.2022.811197
- Yu X, Hong W, Ye M, Lai M, Shi C, Li L, et al. Atypical primary central nervous system lymphoma and glioblastoma: multiparametric differentiation based on non-enhancing volume, apparent diffusion coefficient, and arterial spin labeling. *Eur Radiol*. (2023) 33:5357–67. doi: 10.1007/s00330-023-09681-2
- Lin X, Lee M, Buck O, Woo KM, Zhang Z, Hatzoglou V, et al. Diagnostic accuracy of T1-weighted dynamic contrast-enhanced-MRI and DWI-ADC for differentiation of glioblastoma and primary CNS lymphoma. *AJNR Am J Neuroradiol*. (2017) 38:485–91. doi: 10.3174/ajnr.A5023
- Choi YS, Lee HJ, Ahn SS, Chang JH, Kang SG, Kim EH, et al. Primary central nervous system lymphoma and atypical glioblastoma: differentiation using the initial area under the curve derived from dynamic contrast-enhanced MR and the apparent diffusion coefficient. *Eur Radiol*. (2017) 27:1344–51. doi: 10.1007/s00330-016-4484-2
- Abdel Razek AAK, El-Serougy L, Abdelsalam M, Gaballa G, Talaat M. Differentiation of primary central nervous system lymphoma from glioblastoma: quantitative analysis using arterial spin labeling and diffusion tensor imaging. *World Neurosurg*. (2019) 123:e303–9. doi: 10.1016/j.wneu.2018.11.155
- Zhang H, Schneider T, Wheeler-Kingshott CA, Alexander DC. NODDI: practical *in vivo* neurite orientation dispersion and density imaging of the human brain. *NeuroImage*. (2012) 61:1000–16. doi: 10.1016/j.neuroimage.2012.03.072
- Würtemberger U, Diebold M, Rau A, Akgun V, Becker L, Beck J, et al. Advanced diffusion imaging reveals microstructural characteristics of primary CNS lymphoma, allowing differentiation from glioblastoma. *Neurooncol Adv*. (2024) 6:vdae093. doi: 10.1093/oaajnl/vdae093
- Guo H, Liu J, Hu J, Zhang H, Zhao W, Gao M, et al. Diagnostic performance of gliomas grading and IDH status decoding A comparison between 3D amide proton transfer APT and four diffusion-weighted MRI models. *J Magn Reson Imaging*. (2022) 56:1834–44. doi: 10.1002/jmri.28211
- Xu X, Zhang P, Zhuo Z, Duan Y, Qu L, Cheng D, et al. Prediction of H3K27M alteration status in brainstem glioma using multi-shell diffusion MRI metrics. *J Magn Reson Imaging*. (2024) 60:576–85. doi: 10.1002/jmri.29104
- Qi J, Wang P, Zhao G, Gao E, Zhao K, Gao A, et al. Histogram analysis based on neurite orientation dispersion and density MR imaging for differentiation between glioblastoma multiforme and solitary brain metastasis and comparison of the diagnostic performance of two ROI placements. *J Magn Reson Imaging*. (2023) 57:1464–74. doi: 10.1002/jmri.28419
- Bai J, He M, Gao E, Yang G, Yang H, Dong J, et al. Radiomic texture analysis based on neurite orientation dispersion and density imaging to differentiate glioblastoma from solitary brain metastasis. *BMC Cancer*. (2023) 23:1231. doi: 10.1186/s12885-023-11718-0
- Zhao K, Gao A, Gao E, Qi J, Chen T, Zhao G, et al. Multiple diffusion metrics in differentiating solid glioma from brain inflammation. *Front Neurosci*. (2023) 17:1320296. doi: 10.3389/fnins.2023.1320296
- Navarria P, Pessina F, Clerici E, Bellu L, Franzese C, Franzini A, et al. Re-irradiation for recurrent high grade glioma (HGG) patients: results of a single arm prospective phase 2 study. *Radiother Oncol*. (2022) 167:89–96. doi: 10.1016/j.radonc.2021.12.019
- Xie S, Chen L, Zuo N, Jiang T. DiffusionKit: a light one-stop solution for diffusion MRI data analysis. *J Neurosci Methods*. (2016) 273:107–19. doi: 10.1016/j.jneumeth.2016.08.011
- Garyfallidis E, Brett M, Amirbekian B, Rokem A, van der Walt S, Descoteaux M, et al. Dipy, a library for the analysis of diffusion MRI data. *Front Neuroinform*. (2014) 8:8. doi: 10.3389/fninf.2014.00008
- Yushkevich PA, Piven J, Hazlett HC, Smith RG, Ho S, Gee JC, et al. User-guided 3D active contour segmentation of anatomical structures: significantly improved efficiency and reliability. *NeuroImage*. (2006) 31:1116–28. doi: 10.1016/j.neuroimage.2006.01.015
- Pope WB, Kim HJ, Huo J, Alger J, Brown MS, Gjertson D, et al. Recurrent glioblastoma multiforme: ADC histogram analysis predicts response to bevacizumab treatment. *Radiology*. (2009) 252:182–9. doi: 10.1148/radiol.2521081534
- Su C, Jiang J, Liu C, Shi J, Li S, Chen X, et al. Comparison of amide proton transfer imaging and magnetization transfer imaging in revealing glioma grades and proliferative activities: a histogram analysis. *Neuroradiology*. (2021) 63:685–93. doi: 10.1007/s00234-020-02547-0
- Song YK, Li XB, Huang XL, Zhao J, Zhou XX, Wang YL, et al. A study of neurite orientation dispersion and density imaging in Wilson's disease. *J Magn Reson Imaging*. (2018) 48:423–30. doi: 10.1002/jmri.25930
- Pines AR, Cieslak M, Larsen B, Baum GL, Cook PA, Adebimpe A, et al. Leveraging multi-shell diffusion for studies of brain development in youth and young adulthood. *Dev Cogn Neurosci*. (2020) 43:100788. doi: 10.1016/j.dcn.2020.100788
- Toh CH, Castillo M, Wong AM, Wei KC, Wong HF, Ng SH, et al. Primary cerebral lymphoma and glioblastoma multiforme: differences in diffusion characteristics evaluated with diffusion tensor imaging. *AJNR Am J Neuroradiol*. (2008) 29:471–5. doi: 10.3174/ajnr.A0872
- Haopeng P, Xuefei D, Yan R, Zhenwei Y, Wei H, Ziyin W, et al. Diffusion kurtosis imaging differs between primary central nervous system lymphoma and high-grade glioma and is correlated with the diverse nuclear-to-cytoplasmic ratio: a histopathologic, biopsy-based study. *Eur Radiol*. (2020) 30:2125–37. doi: 10.1007/s00330-019-06544-7
- Smits M, van den Bent MJ. Imaging correlates of adult glioma genotypes. *Radiology*. (2017) 284:316–31. doi: 10.1148/radiol.2017151930
- Guo AC, Cummings TJ, Dash RC, Provenzale JM. Lymphomas and high-grade astrocytomas: comparison of water diffusibility and histologic characteristics. *Radiology*. (2002) 224:177–83. doi: 10.1148/radiol.2241010637
- Yu X, Gebre RK, Przybelski SA, Reid RI, Raghavan S, Lesnick TG, et al. NODDI may be more sensitive to neurodegenerative changes than structural MRI. *Alzheimers Dement*. (2023) 19:e076509. doi: 10.1002/alz.076509
- Zerweck L, Würtemberger U, Klose U, Reiser M, Richter V, Nagele T, et al. Performance comparison of diffusion kurtosis imaging (DKI), neurite orientation dispersion and density imaging (NODDI), and diffusion microstructure imaging (DMI) in predicting adult-type glioma subtype—a pilot study. *Cancers*. (2025) 17:876. doi: 10.3390/cancers17050876
- Gao A, Zhang H, Yan X, Wang S, Chen Q, Gao E, et al. Whole-tumor histogram analysis of multiple diffusion metrics for glioma genotyping. *Radiology*. (2022) 302:652–61. doi: 10.1148/radiol.210820
- Jiang R, Hu X, Deng K, Jiang S, Chen W, Zhang Z. Neurite orientation dispersion and density imaging in evaluation of high-grade glioma-induced corticospinal tract injury. *Eur J Radiol*. (2021) 140:109750. doi: 10.1016/j.ejrad.2021.109750
- Bai J, He M, Gao E, Yang G, Zhang C, Yang H, et al. High-performance presurgical differentiation of glioblastoma and metastasis by means of multiparametric neurite orientation dispersion and density imaging (NODDI) radiomics. *Eur Radiol*. (2024) 34:6616–28. doi: 10.1007/s00330-024-10686-8
- Figini G, Castellano A, Bailo M, Callea M, Cadioli M, Bouyagoub S, et al. Comprehensive brain tumour characterisation with VERDICT-MRI: evaluation of cellular and vascular measures validated by histology. *Cancers*. (2023) 15:2490. doi: 10.3390/cancers15092490
- Liu K, Lin Z, Zheng T, Ba R, Zhang Z, Li H, et al. Improving microstructural estimation in time-dependent diffusion MRI with a Bayesian method. *J Magn Reson Imaging*. (2025) 61:724–34. doi: 10.1002/jmri.29434
- Wang P, Gao E, Qi J, Ma X, Zhao K, Bai J, et al. Quantitative analysis of mean apparent propagator-magnetic resonance imaging for distinguishing glioblastoma from solitary brain metastasis. *Eur J Radiol*. (2022) 154:110430. doi: 10.1016/j.ejrad.2022.110430
- Tan Y, Wang XC, Zhang H, Wang J, Qin JB, Wu XF, et al. Differentiation of high-grade-astrocytomas from solitary-brain-metastases: comparing diffusion kurtosis imaging and diffusion tensor imaging. *Eur J Radiol*. (2015) 84:2618–24. doi: 10.1016/j.ejrad.2015.10.007
- Wang X, Liu X, Chen Y, Lin G, Mei W, Chen J, et al. Histopathological findings in the peritumoral edema area of human glioma. *Histol Histopathol*. (2015) 30:1101–9. doi: 10.14670/HH-11-607
- Oh J, Cha S, Aiken AH, Han ET, Crane JC, Stainsby JA, et al. Quantitative apparent diffusion coefficients and T2 relaxation times in characterizing contrast enhancing brain tumors and regions of peritumoral edema. *J Magn Reson Imaging*. (2005) 21:701–8. doi: 10.1002/jmri.20335
- Wang P, Shi YH, Li JY, Zhang CZ. Differentiating glioblastoma from primary central nervous system lymphoma: the value of shaping and nonenhancing peritumoral hyperintense gyral lesion on FLAIR imaging. *World Neurosurg*. (2021) 149:e696–704. doi: 10.1016/j.wneu.2021.01.114